


# Topological Chiral and Nematic Superconductivity by Doping Mott Insulators on Triangular Lattice

Yixuan Huang<sup>1</sup> and D. N. Sheng<sup>1\*</sup>

*Department of Physics and Astronomy, California State University, Northridge, California 91330, USA*

 (Received 4 January 2022; revised 25 May 2022; accepted 22 June 2022; published 14 July 2022)

The mechanism of unconventional topological superconductivity (TSC) remains a long-standing issue. We investigate the quantum phase diagram of the extended  $t$ - $J$ - $J_\chi$  model including spin chiral interactions on triangular lattice based on state-of-the-art density matrix renormalization group simulations. We identify distinct classes of superconducting phases characterized by nonzero topological Chern numbers  $C = 1$  and  $2$  and a nematic  $d$ -wave superconducting phase with a zero Chern number. The TSC states are shown to emerge from doping either a magnetic insulator or chiral spin liquid, which opens new opportunities for experimental discovery. In addition, we further classify the  $C = 2$  class of TSC phases into an isotropic and a nematic TSC phase and present evidence of continuous quantum phase transitions from the nematic TSC phase to both isotropic TSC and nematic  $d$ -wave phases. These results provide new insight into the mechanism of TSC with an emphasis on the role played by hole dynamics, which changes spin background and drives a topological phase transition at a hole doping level around 3% upon doping a magnetic insulator to enable the emergence of TSC.

DOI: [10.1103/PhysRevX.12.031009](https://doi.org/10.1103/PhysRevX.12.031009)

Subject Areas: Strongly Correlated Materials,  
Superconductivity,  
Topological Insulators

## I. INTRODUCTION

There have been intensive studies of the canonical models for strongly correlated systems, the two-dimensional (2D) Hubbard and  $t$ - $J$  models, and their generalized versions since the discovery of high- $T_c$  cuprate superconductivity (SC) [1–7]. At the strong coupling limit, these models host different Mott insulating states varying from magnetic insulators to spin liquids [8]. Understanding the interplay of conventional orders, spin liquid physics, and unconventional SC in doped Mott insulators is one of the central challenges of condensed matter physics. A large body of work on unconventional SC is connected to the original proposal of the resonating valence bond theory [1] that doping Mott insulators might naturally lead to SC [2,5,6,9–11]. Lacking well-controlled analytical solutions in 2D with strong couplings, unbiased numerical studies play an important role in establishing the quantum phases in such models. Along this direction, exciting progress has been made in understanding the emergence of SC and its interplay with spin fluctuations and charge stripes by

doping the antiferromagnetic Mott state on square lattice based on extensive numerical simulations [12–23], which is relevant to cuprate SC. In particular, more recent density matrix renormalization group (DMRG) [24] studies have established robust SC for extended  $t$ - $J$  and Hubbard models on square lattice with next-nearest-neighbor hoppings, suggesting the importance of tuning hole dynamics to enhance SC [15,21–23].

Mott insulating states on triangular lattice offer another exciting playground and challenges for their distinct interplay between geometric frustrations, lattice rotational symmetry, and quantum fluctuations [7,11,25–40]. On the experimental side, the SC state observed in  $\text{Na}_x\text{CoO}_2 \cdot y\text{H}_2\text{O}$  might be a  $d + id$ -wave topological superconductivity (TSC) state which breaks time-reversal symmetry [41,42]. More recently, different twisted transition metal dichalcogenide (TMD) moiré systems have been discovered to be quantum simulators of the Hubbard model [43,44], which are promising systems hosting correlated insulators and topological superconductors [45–47].

Theoretically, the Kalmeyer-Laughlin (KL) chiral spin liquid (CSL) [48,49] has been identified among the phase boundaries of different competing magnetic ordered states [50–54] for frustrated spin systems or near the Mott transition for the Hubbard model [36,37] on triangular lattice. Whether doping a KL CSL can generally lead to the TSC [11,32,34,48,49,55–57] remains an open question. A recent theoretical study [11] suggests that doping a KL CSL

\*[donna.sheng1@csun.edu](mailto:donna.sheng1@csun.edu)

*Published by the American Physical Society under the terms of the Creative Commons Attribution 4.0 International license. Further distribution of this work must maintain attribution to the author(s) and the published article's title, journal citation, and DOI.*

may naturally lead to a chiral metal, while a topological  $d + id$ -wave SC represents a more nontrivial scenario requiring the internal gauge flux to be adjusted with the hole doping level. Indeed, unbiased numerical simulations have found a possible chiral metal by doping the CSL identified at half filling of the triangular Hubbard model [34,36]. The nontrivial example of identifying the topological  $d + id$ -wave SC by doping the KL CSL comes from the study of the  $t$ - $J$ - $J_\chi$  model [32] with strong three-spin chiral interactions. The topological class of the observed TSC state [32] characterized by a finite integer quantized spin Chern number [58,59] and chiral Majorana edge modes has not been revealed. Crucially, the driving mechanism for the emergence of the TSC remains to be identified, which may require extensive exploration in the parameter space by tuning relevant hopping parameters and interactions [32,53,54]. Given the fact that CSLs often emerge near the boundaries between different magnetically ordered states [53,54], related open questions naturally arise including what the interplay is between TSC and conventional orders or fluctuations and whether distinct unconventional SC states can emerge by doping different magnetically ordered states.

To address these open issues, we study the quantum phase diagram and focus on the emergent unconventional SC in the extended  $t$ - $J$ - $J_\chi$  model on triangular lattice based on large-scale DMRG simulations [24]. By tuning the ratios of the next-nearest- and nearest-neighbor hoppings ( $t_2/t_1$ ) and Heisenberg spin couplings ( $J_2/J_1$ ) in the presence of three spin chiral interactions ( $J_\chi$ ) [32], we identify different superconducting phases including distinct  $d + id$ -wave TSC phases that are characterized by nonzero topological Chern numbers  $C = 1$  and  $2$  and a nematic SC phase with a  $d$ -wave pairing symmetry breaking lattice rotational symmetry and  $C = 0$ . Furthermore, for weaker  $J_\chi$  the  $C = 2$  phases include isotropic and nematic TSC phases with a continuous quantum phase transition between them. We demonstrate that these topological and nematic  $d$ -wave SC states have robust power-law-decaying pairing correlations in the form of Luther-Emery liquid [60] on wider cylinders, which may lead to different superconducting states in 2D. The TSC can be induced by either doping a magnetically ordered state or CSL, which provides a new opportunity for experimental discovery of unconventional TSC. We also demonstrate the important role played by hole dynamics, which can drive a topological phase transition upon doping a  $120^\circ$  antiferromagnetic (AFM) state at a hole doping level  $\delta \approx 3\%$ , enabling the TSC to emerge. Furthermore, nematic SC with  $C = 0$  can emerge from either doping the CSL or magnetic ordered states [53], suggesting the rich interplay between unconventional SC and spin background.

The rest of the paper is organized as follows. In Sec. II, we introduce the extended  $t$ - $J$ - $J_\chi$  model on triangle lattice, the DMRG method, and the topological characterization for

the SC states through spin flux insertion. Its quantum phase diagram is presented in Sec. III, containing different TSC phases and a nematic  $d$ -wave SC phase. We demonstrate their distinct topological Chern numbers (Sec. III A), the quasi-long-range order in SC pairing correlations (Sec. III B), and the pairing symmetries (Sec. III C) to characterize these phases. In Sec. IV, we focus on the quantum phase transitions by tuning the ratios of  $t_2/t_1$  and  $J_2/J_1$ , with Sec. IV A showing the evolution of SC pairing correlations, Sec. IV B addressing the nature of quantum phase transitions among different phases, and Sec. IV C showing the evolution of spin correlations. The summary and discussions are presented in Sec. V.

## II. MODEL AND METHOD

We study the extended  $t$ - $J$ - $J_\chi$  model that is defined as

$$H = - \sum_{\{ij\},\sigma} t_{ij} (\hat{c}_{i,\sigma}^\dagger \hat{c}_{j,\sigma} + \text{H.c.}) + \sum_{\{ij\}} J_{ij} \left( \hat{S}_i \cdot \hat{S}_j - \frac{1}{4} \hat{n}_i \hat{n}_j \right) + J_\chi \sum_{\{ijk\} \in \nabla/\Delta} \hat{S}_i \cdot (\hat{S}_j \times \hat{S}_k), \quad (1)$$

where  $\hat{c}_{i,\sigma}^\dagger$  is the electron creation operator on site  $i$  with spin index  $\sigma = \pm 1$ ,  $\hat{S}_i$  is the spin- $\frac{1}{2}$  operator, and  $\hat{n}_i = \sum_\sigma \hat{c}_{i,\sigma}^\dagger \hat{c}_{i,\sigma}$  is the electron number operator. We consider the nearest-neighbor and the next-nearest-neighbor hoppings  $t_1$  and  $t_2$  as well as Heisenberg couplings  $J_1$  and  $J_2$ , supplemented by the three-spin chiral interactions  $J_\chi$  on every elementary triangle as illustrated in Fig. 1(a). The chiral interaction can be generated from the Hubbard model with an external magnetic field [32]. We set  $J_1 = 1$  as the unit of energy,  $t_1 = 3$ ,  $J_2/J_1 = (t_2/t_1)^2$ , and focus on the regime of  $0 < J_2, J_\chi \leq 0.2$  with hole doping level  $\delta \leq 1/8$ , which is the optimal doping region for unconventional SC [22,32].

To obtain the ground state of the Hamiltonian in Eq. (1), we apply the DMRG method with  $U(1) \times SU(2)$  for charge and spin symmetries [61] on cylinder systems with an open boundary condition along the axis ( $e_a$  or  $x$ -) direction and a periodic boundary condition along the circumferential ( $e_b$  or  $y$ -) direction, as illustrated in Fig. 1(a). The number of sites is  $N = L_x \times L_y$ , where  $L_x$  and  $L_y$  denote the lengths in these two directions, respectively. The number of electrons  $N_e$  is related to the doping level  $N_e/N = 1 - \delta$ . We keep up to  $M = 12\,000$   $SU(2)$  spin multiplets [equivalent to about  $m = 36\,000$   $U(1)$  states] with truncation error  $\epsilon \sim 10^{-6}$ , which leads to accurate results (see Supplemental Sec. II [62] for details). We develop a topological characterization for the SC states through the spin flux insertion by adiabatically evolving the ground state as a function of a twisted boundary phase  $\theta_F$  based on the method established for CSL and fractional quantum Hall systems [52,63]. The flux adds a spin-dependent phase factor to the electron

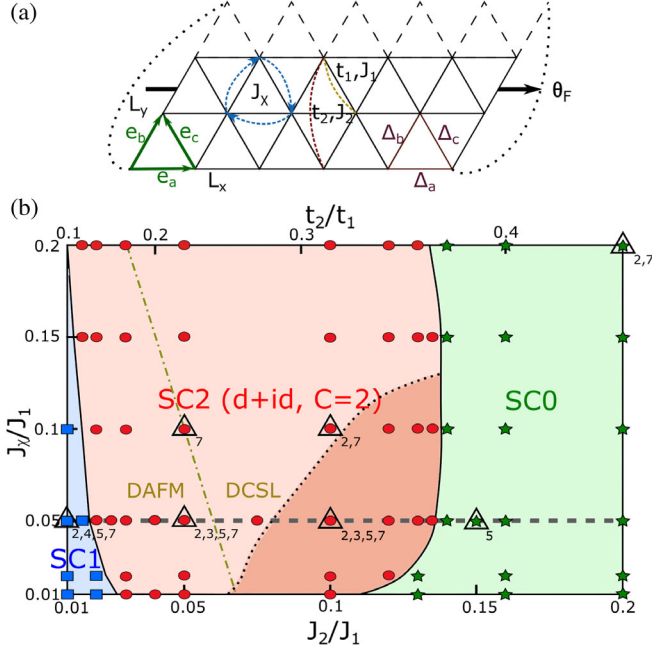


FIG. 1. Quantum phase diagram. (a) Schematic illustration of the extended  $t$ - $J$ - $J_\chi$  model on triangle lattice with the nearest-neighbor and the next-nearest-neighbor hoppings  $t_1$  and  $t_2$  and Heisenberg exchange  $J_1$  and  $J_2$  interactions, as well as the three-spin chiral interactions  $J_\chi$ . The dashed lines indicate the periodic boundary condition. (b) The quantum phase diagram obtained on  $L_y = 6$  cylinders based on the Chern number simulations. For  $0.01 \leq J_2/J_1, J_\chi/J_1 \leq 0.2$ , and doping level  $\delta = 1/12$ , we identify distinct classes of SC phases labeled as SC1, SC2, and SC0 from left to right characterized by their spin Chern number  $C$ . The SC2 regime represents two phases: the isotropic TSC (lighter red region) and nematic TSC (darker red region) phases. Different symbols represent parameter points studied with the DMRG methods. The triangles mark points presented in the paper with the lower indices representing the indices of figures. A scan of the Chern number, SC pairing symmetry, and energy or entropy along the horizontal dashed line is used in Figs. 2(c), 5(d), and 6, respectively. The main feature of the phase diagram is essentially the same for other doping levels  $\delta = 1/24$ – $1/8$ .

hoppings  $\hat{c}_{i,\sigma}^\dagger \hat{c}_{j,\sigma} \rightarrow e^{i\sigma\theta_F} \hat{c}_{i,\sigma}^\dagger \hat{c}_{j,\sigma}$  if  $j \rightarrow i$  crossing the  $y$  boundary from the top [see Fig. 1(a)] and similarly couples to the spin flip terms [52]. In this type of calculation,  $SU(2)$  symmetry is broken by the spin flux and we use  $U(1) \times U(1)$  symmetries with bond dimensions up to  $m = 8000$  for accurate results due to the robustness of the topologically protected spin pumping (see Supplemental Sec. I [62] for more details).

### III. QUANTUM PHASE DIAGRAM

At half filling (with no doping  $\delta = 0$ ), the Hamiltonian in Eq. (1) reduces to the Heisenberg  $J_1$ - $J_2$ - $J_\chi$  model [53]. In the small  $J_2$  regime ( $J_1 = 1$ ), the  $120^\circ$  AFM order survives up to  $J_2 \approx 0.07$  at  $J_\chi = 0$ , which smoothly extends to the

nonzero  $J_\chi$  regime. The intermediate  $J_2$  regime is dominated by the CSL, which separates from the AFM order by the dash-dotted line as shown in Fig. 1(b) obtained from Refs. [53,54]. Through extensive DMRG simulations of topological Chern numbers and SC pairing correlations on  $L_y = 4$ – $6$  cylinders for hole-doped systems, we establish a quantum phase diagram in the parameter space  $0 < J_2, J_\chi \leq 0.2$  for doping  $\delta = 1/12$ , with three distinct classes of superconducting phases stabilized by small  $J_2, J_\chi \geq 0.01$  [64] as shown in Fig. 1(b). These SC phases are characterized by different topological spin Chern numbers. At small  $J_2$ , we find a topological chiral  $d + id$ -wave SC phase with spin Chern number  $C = 1$  (labeled as SC1) by doping the AFM (DAFM) state. In the intermediate  $J_2$  regime, another class of topological  $d + id$ -wave SC phases emerges characterized by a quantized  $C = 2$  (SC2), which can be induced by doping either the AFM state or the CSL (DCSL) as illustrated in Fig. 1(b). The SC2 class is further divided into an isotropic TSC phase and a nematic TSC phase breaking rotational symmetry. Interestingly, the nematic TSC state is an analog state of the recently revealed nematic fractional quantum Hall effect [65–68]. At larger  $J_2$ , the SC phase has  $d$ -wave symmetry with anisotropic pairing correlations breaking the lattice rotational symmetry and  $C = 0$  (SC0) indicating a topologically trivial SC phase. The SC0 phase belongs to the same quantum phase as the nematic  $d$ -wave SC identified for an extended  $t$ - $J$  model [33] with time-reversal symmetry. The phase diagram is essentially the same for other doping levels  $\delta = 1/24$ – $1/8$  with small shifts in phase boundaries (e.g., at  $\delta = 1/8$ ,  $\Delta J_{2c}^{(1)} \approx 0.01$ – $0.02$ , where  $J_{2c}^{(1)}$  denotes the critical  $J_2$  between SC1 and SC2). We also find that the previously revealed  $d + id$ -wave SC state (at  $J_\chi = 0.4$  and  $J_2 = t_2 = 0.0$ ) [32] has  $C = 2$  sitting near the phase boundary of the SC2 phase.

#### A. Topological Chern number characterization through flux insertion

The nonzero Chern number characterizes the topological nature of the  $d + id$ -wave superconductors [58,59], which also identifies the number of chiral Majorana edge modes. We determine the spin Chern number through the spin pumping with inserting flux  $\theta_F$  into the cylinder, as illustrated in Fig. 1(a). The net spin with nonzero  $S_z$  accumulates near the boundaries of the cylinder as the flux adiabatically increases, while the total  $S_z = 0$  for the ground state at different  $\theta_F$ . We use a small step for the increase of the flux  $\theta_F \rightarrow \theta_F + \Delta\theta_F$  with  $\Delta\theta_F = 2\pi/16$ . A finite Chern number [52] can be obtained from the total spin pumping  $C = \Delta Q_s |_{0}^{2\pi} = (n_\uparrow - n_\downarrow) |_{0}^{2\pi}$  measured at the left boundary at  $\theta_F = 0$  and  $2\pi$ , where  $n_\sigma$  is the accumulated charge near the boundary with spin  $\sigma$ . We directly measure the pumped spin for each  $\theta_F$  from the reduced density matrix by calculating the sum  $Q_s = \sum_\alpha \lambda_\alpha (n_{\uparrow,\alpha} - n_{\downarrow,\alpha})$ , where  $\lambda_\alpha$  is the

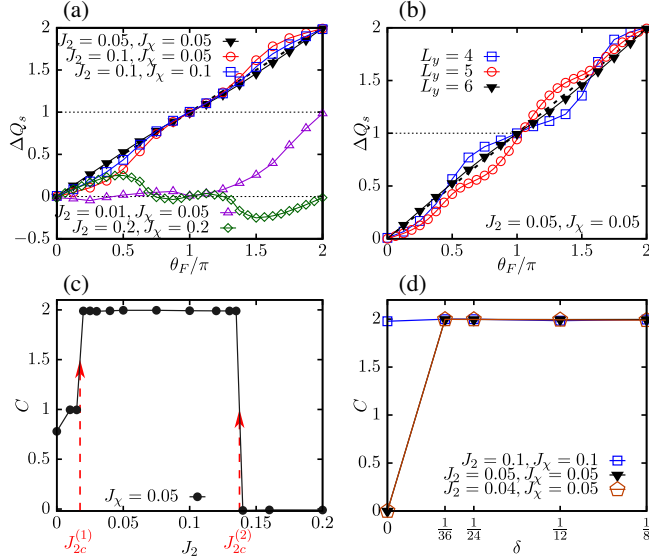


FIG. 2. The pumped spin by inserting flux and spin Chern number. (a) The pumped spin  $\Delta Q_s$  with adiabatically inserted flux  $\theta_F$  is shown for different SC phases on the  $L_y = 6$  cylinder. For the three parameter points in the SC2 phase, the measured spin pumping after inserting one flux quantum  $\Delta Q_s|_0^{2\pi} = 1.993, 1.983, 1.990$ , respectively, indicating that the error bar is around 1% from the exactly quantized value  $\Delta Q_s|_0^{2\pi} = 2$  for different systems. (b)  $\Delta Q_s$  versus  $\theta_F$  for  $J_2 = J_\chi = 0.05$  inside SC2 phase on  $L_y = 4, 5, 6$  cylinders. (c) The evolution of Chern number  $C$  with varying  $J_2$  at  $J_\chi = 0.05$  on  $L_y = 6$ .  $C = \Delta Q_s|_0^{2\pi}$  is obtained after inserting one flux quantum  $\theta_F = 0 \rightarrow 2\pi$ . SC1-SC2 and SC2-SC0 phase transitions take place at  $J_2 = J_{2c}^{(1)}$  and  $J_{2c}^{(2)}$ , respectively, where the Chern number jumps. The doping level is  $\delta = 1/12$  for (a)–(c). (d)  $C$  versus  $\delta$  for parameter points with different undoped parent states (e.g., DAFM or DCSL) on  $L_y = 6$ .

eigenvalue and  $\alpha$  the eigenstate of the reduced density matrix [63] and  $n_{\uparrow,\alpha}$  ( $n_{\downarrow,\alpha}$ ) is the particle number of the  $\alpha$  state with up (down) spin. Because the inserted flux breaks  $SU(2)$  symmetry, we use infinite DMRG with  $U(1) \times U(1)$  symmetries with a large unit cell that is commensurate with the doping level (see Supplemental Sec. I [62]).

We show examples of the flux insertion and the resulting Chern numbers for systems with  $\delta = 1/12$  in Fig. 2(a). For three parameter points inside the SC2 phase on the  $L_y = 6$  system, the  $\Delta Q_s$  increases almost linearly with  $\theta_F$ , indicating uniform Berry curvature [69], and there is  $\Delta Q_s \approx 2.0$  net spin pumped to the boundary after the threading of one flux quantum ( $\theta_F = 0 \rightarrow 2\pi$ ). This corresponds to the quantized Chern number  $C = 2$ , which remains the same on various  $L_y = 4, 5$ , and  $6$  as shown in Fig. 2(b). The pumping rate becomes more uniform with the increase of  $L_y$ , indicating the increased robustness of the topological quantization for larger systems. In contrast, at  $J_2 = 0.01, J_\chi = 0.05$  inside the SC1 phase, we find no linear relation between  $\Delta Q_s$  and  $\theta_F$ , which indicates the

nonuniform Berry curvature versus boundary phase  $\theta_F$  [69]. The measured  $\Delta Q_s \approx 0.983$ , indicating around one net spin pumped with the insertion of one flux quantum and  $C = 1$ . The Chern number becomes nonquantized extended to the  $J_2 = 0$  limit as shown in Fig. 2(c), signaling gapless low-energy excitations. We believe the large variance of the Berry curvature versus  $\theta_F$  for the SC1 phase may indicate a topological state with gapless excitations at small  $J_2$  consistent with an early proposal for a topological superconducting state for the  $\text{Na}_x\text{CoO}_2 \cdot y\text{H}_2\text{O}$  system based on variational simulations [42]. In the SC0 phase at larger  $J_2 = J_\chi = 0.2$ , we find  $\Delta Q_s \approx -0.01$ , which confirms  $C = 0$  for a topologically trivial SC state. Thus, the phase transitions between the three phases can be characterized by jumps of topological Chern number  $C$  with varying  $J_2$  at a fixed  $J_\chi = 0.05$  as illustrated in Fig. 2(c).

Since the undoped ( $\delta = 0$ ) parent state of the SC2 phase contains both the AFM state and CSL, a natural question is how the Chern number evolves with the doping level. As demonstrated in Fig. 2(d), for two points in the DAFM regime at  $J_2 = 0.04, 0.05$  and  $J_\chi = 0.05$ ,  $C$  jumps from 0 to 2 at a small doping of  $\delta = 1/36$  and remains quantized at  $C = 2$  for larger  $\delta$ , which demonstrates a doping-induced topological quantum phase transition. On the contrary, in the DCSL regime at  $J_2 = J_\chi = 0.1$ ,  $C = 2$  for  $\delta = 0-1/8$ , which shows a robust Chern number quantization from the parent CSL to the topological  $d + id$ -wave SC. This is consistent with the fact that the KL CSL is a bosonic  $\nu = 1/2$  fractional quantum Hall state [48,49,58], which is equivalent to the  $C = 2$  topological order for fermionic systems where the phase space is enlarged by a factor of 4 in the definition of the Chern number [70] with a doubled flux period for the Hamiltonian to be invariant. The exact quantization  $C = 2$  of the SC2 phase indicates that doped holes can indeed adjust the internal flux with the hole doping level to realize a bosonic integer quantum Hall effect for holons [11].

## B. Quasi-long-range order in superconducting pairing correlations

To explore the superconducting nature of the system, we focus on the dominant spin singlet pairing correlations  $P_{\alpha\beta}(\mathbf{r}) = \langle \hat{\Delta}_\alpha^\dagger(\mathbf{r}_0) \hat{\Delta}_\beta(\mathbf{r}_0 + \mathbf{r}) \rangle$ , where the pairing operator  $\hat{\Delta}_\alpha(\mathbf{r}) = (\hat{c}_{\mathbf{r}\uparrow} \hat{c}_{\mathbf{r}+e_a\downarrow} - \hat{c}_{\mathbf{r}\downarrow} \hat{c}_{\mathbf{r}+e_a\uparrow})/\sqrt{2}$  with  $\alpha = a, b, c$ , representing different nearest-neighboring bonds as illustrated in Fig. 1(a).

We first give an example of the SC pairing correlations in the SC2 regime as shown in Fig. 3(a), where the magnitude of pairing correlations at longer distance for two  $b$  bonds (along the  $y$  direction)  $|P_{bb}(r)|$  increases gradually as the DMRG bond dimension increases from  $M = 6000$  to  $12000$  at  $J_2 = 0.1, J_\chi = 0.05$  on the  $N = 36 \times 6$  system. Because the DMRG represents the ground state in the matrix product form [71] with finite bond dimensions, the

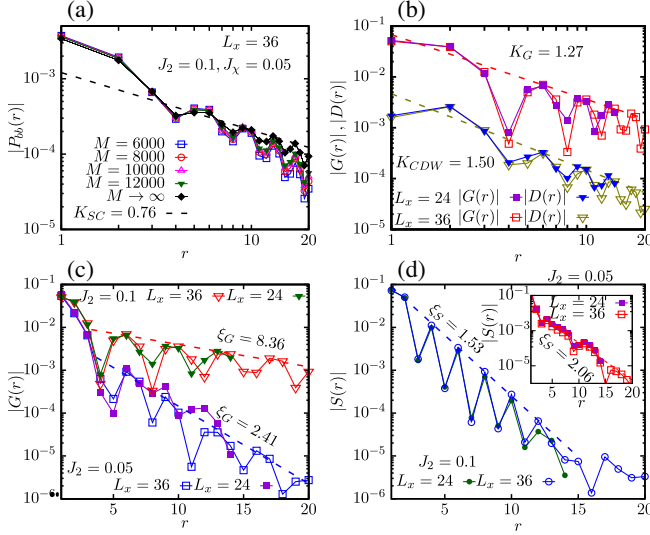


FIG. 3. Pairing and other correlations in SC2. (a) The SC pairing correlations for different bond dimensions  $M$  at  $J_2 = 0.1, J_\chi = 0.05$  for the  $N = 36 \times 6$  system.  $\mathbf{r}$  is chosen along the  $x$  direction  $\mathbf{r} = (r, 0)$ , and the reference point is  $\mathbf{r}_0 = (L_x/4, y_0)$  to avoid the boundary effect (the results are independent of  $y_0$  because of the translational invariant along the  $y$  direction). The straight-line fit in the log-log plot of the extrapolated data in the infinite  $M$  limit follows a power-law behavior. (b) The density-density correlation  $|D(r)|$  and single-particle correlation  $|G(r)|$  which are fit by the power-law relation for  $N = 24 \times 6$  and  $36 \times 6$ , at  $J_2 = 0.1, J_\chi = 0.05$ . (c) The comparison of  $|G(r)|$  at  $J_2 = 0.05$  and  $0.1$  with the same  $J_\chi = 0.05$ , which demonstrates the fast growing of the correlation length  $\xi_G$  with the increase of  $J_2$ . (d) The exponential decay of the spin correlations  $|S(r)|$  in the main figure and its inset for the same parameters as in (c), where  $r > 15$  data points are ignored in the fitting, because their values are comparable to the numerical truncation error. The doping level is  $\delta = 1/12$ . The obtained fitting exponents or correlation lengths have error bars around 0.02, except for the one in the inset in (d), which is around 0.06.

scaling to  $M \rightarrow \infty$  is needed to identify the true nature of long-distance correlations for wider cylinders. Using a second-order polynomial fitting of  $1/M$ , we find that the extrapolated  $|P_{bb}(r)|$  shows a power-law decay with distance  $|P_{bb}(r)| \sim r^{-K_{SC}}$ , with the Luttinger exponent  $K_{SC} \approx 0.76$ . Similar results are obtained for correlations with other bonds and also for different  $L_x$  or  $L_y = 4$  systems (see Supplemental Sec. III A [62]).  $K_{SC} \lesssim 1$  holds for the SC2 phase, indicating a strong divergent SC susceptibility in the zero-temperature limit [33].

We then turn to the density-density  $D(\mathbf{r}) = \langle \hat{n}_{\mathbf{r}_0} \hat{n}_{\mathbf{r}_0+\mathbf{r}} \rangle - \langle \hat{n}_{\mathbf{r}_0} \rangle \langle \hat{n}_{\mathbf{r}_0+\mathbf{r}} \rangle$  and single-particle  $G(\mathbf{r}) = \sum_{\sigma} \langle \hat{c}_{\mathbf{r}_0, \sigma}^\dagger \hat{c}_{\mathbf{r}_0+\mathbf{r}, \sigma} \rangle$  correlations. As shown in Fig. 3(b), the  $|D(r)|$  decays with a power-law relation at long distance using extrapolated data. The Luttinger exponent for density-density correlations is  $K_{CDW} \approx 1.50$ , much larger than  $K_{SC}$ . Both  $|P_{bb}(r)|$  and  $|D(r)|$  show similar spatial oscillations consistent with the electron density oscillation in real space (see

Supplemental Sec. V [62]). Similarly, the single-particle Green function  $|G(r)|$  can also be fit into power-law behavior [Fig. 3(b)]. Interestingly, we identify a crossover for  $|G(r)|$  with the increase of  $J_2$ . At smaller  $J_2 = 0.05$  in the SC2 regime, we observe an exponential decay in  $|G(r)|$  with a short correlation length  $\xi_G \approx 2.41$  which is consistent with the gapped isotropic TSC state as shown in Fig. 3(c). With the increase of  $J_2$ , the correlation length for  $|G(r)|$  increases to  $\xi_G \approx 8.36$ , larger than  $L_y$ , which could also be fitted by a power-law decay [as shown in Fig. 3(b)] at  $J_2 = 0.1$  for fixed  $J_\chi = 0.05$  on different systems  $N = 24 \times 6$  and  $36 \times 6$ . The evolution of the single-particle correlation length is a signature of the evolution of the quasiparticle excitation gap, which gradually reduces with the increase of the  $J_2$  approaching the quantum phase transition from a gapped SC state to a nodal nematic SC state as we address further in Sec. IV. In comparison, the spin-spin correlations remain exponentially decay with a short correlation length  $\xi_S \approx 1.53$  (2.06) as shown in the main panel (inset) in Fig. 3(d) at  $J_2 = 0.1$  (0.05), indicating a finite spin gap which protects the SC state. These results provide compelling evidence for the robust SC pairing correlations as dominant correlations for SC phases with  $C = 2$ , which are the quasi-1D descendent states of 2D topological superconductors.

Now we discuss the features of various correlations at small  $J_2$ , where the SC1 phase is identified with the Chern number  $C = 1$ . The SC pairing correlations are shown in Fig. 4(a), where the magnitude of the SC pairing correlations  $|P_{bb}(r)|$  show power-law behavior with the Luttinger exponents  $K_{SC} \approx 1.09$  and  $0.59$  for  $J_2 = 0$  and  $0.01$ , respectively, obtained with a fixed  $J_\chi = 0.05$  for the  $N = 48 \times 4$  system. In comparison, as shown in Fig. 4(b), the  $|D(r)|$  decays with a power-law relation with larger exponents ( $K_{CDW} \approx 1.56$  and  $1.39$ ), while the  $|G(r)|$  [Fig. 4(c)] and  $|S(r)|$  [Fig. 4(d)] both decay exponentially with small correlation lengths. These results indicate that the SC1 phase has dominant SC correlations observed for  $L_y = 4$  cylinders. We also confirm power-law SC correlations for a wider system of  $N = 20 \times 6$  at  $J_2 = 0.01, J_\chi = 0.05$  with good numerical convergence for this possible gapless phase. Interestingly, there are stronger spin correlations for the  $L_y = 6$  system, indicating a vanishing or very small spin gap (see Supplemental Sec. III D [62]), which is consistent with the fact that the SC1 phase has a spin gap-closing transition from the  $C = 2$  phase.

We further confirm that the SC0 phase has robust quasi-long-range SC pairing correlations with a Luttinger exponent  $K_{SC} \approx 1.10$  at  $J_2 = J_\chi = 0.2$  dominating the density-density correlations. This phase can be smoothly connected to the  $d$ -wave phase identified by doping the  $J_1 - J_2$  model [33] with larger  $J_2$  (see Supplemental Sec. III C [62] for more details).

There are other competing quantum phases and additional quantum phase transitions as we reduce the three spin

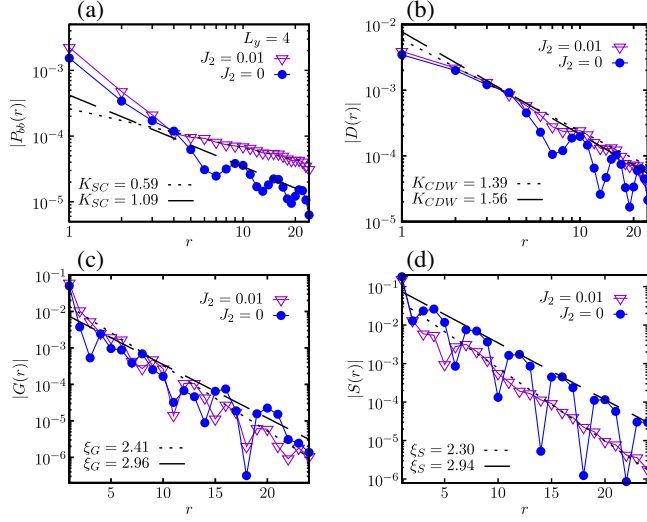


FIG. 4. Pairing and other correlations at  $J_\chi = 0.05$  for smaller  $J_2$  on  $L_y = 4$ . The results are converged with a large bond dimension  $M = 10000$ . (a) The SC pairing correlations.  $\mathbf{r}$  is chosen along the  $x$  direction  $\mathbf{r} = (r, 0)$ , and the reference point is  $\mathbf{r}_0 = (L_x/4, L_y/2)$  to avoid the boundary effect. The straight-line fit in the log-log plot follows a power-law behavior, with exponents of 1.09 and 0.59 for  $J_2 = 0$  and 0.01, respectively. (b) The density-density correlations  $|D(r)|$  which are fit by a power-law relation, with exponents of 1.56 and 1.39 for  $J_2 = 0$  and 0.01, respectively. (c) The single-particle correlations  $|G(r)|$  which are fit by an exponential decay with correlation lengths of 2.96 and 2.41 for  $J_2 = 0$  and 0.01, respectively. (d) The spin correlations  $|S(r)|$  which are fit by an exponential decay with correlation lengths of 2.94 and 2.30 for  $J_2 = 0$  and 0.01, respectively. The doping level is  $\delta = 1/12$ . The obtained fitting exponents or correlation lengths have error bars around 0.03.

chiral interactions to zero in the small  $J_2$  regime. For example, at  $J_2 = J_\chi = 0$ , the ground state is dominated by charge stripe and spin fluctuations with suppressed pairing correlations. Furthermore, additional results for  $L_y = 4$  with small  $J_2$  for a possible pairing density wave SC phase [38] and a  $d$ -wave SC phase coexisting with phase separation are shown in Supplemental Sec. III F [62]. These results provide further support that a small but finite chiral interaction plays an important role in stabilizing the topological SC phases for the systems we study.

### C. Pairing symmetry for topological and nematic SC phases

The SC pairing symmetry can be identified by the phases of the pairing correlations for different bonds. To extract the phase, we rewrite the SC pairing correlation as  $P_{\alpha\beta}(\mathbf{r}) = |P_{\alpha\beta}(\mathbf{r})|e^{i\phi_{\alpha\beta}(\mathbf{r})}$ , where  $\phi_{\alpha\beta}(\mathbf{r})$  is the phase for the correlation, and the pairing order parameter as  $\Delta_\alpha(\mathbf{r}) = |\Delta_\alpha(\mathbf{r})|e^{i\theta_\alpha(\mathbf{r})}$ . Using the definition of the pairing correlations, we obtain  $\theta_{\alpha\beta}(\mathbf{r}) = \theta_\alpha(\mathbf{r}) - \theta_\beta(\mathbf{r}) = \phi_{\alpha\alpha}(\mathbf{r}) - \phi_{\alpha\beta}(\mathbf{r})$  as the relative phases of the pairing order parameters

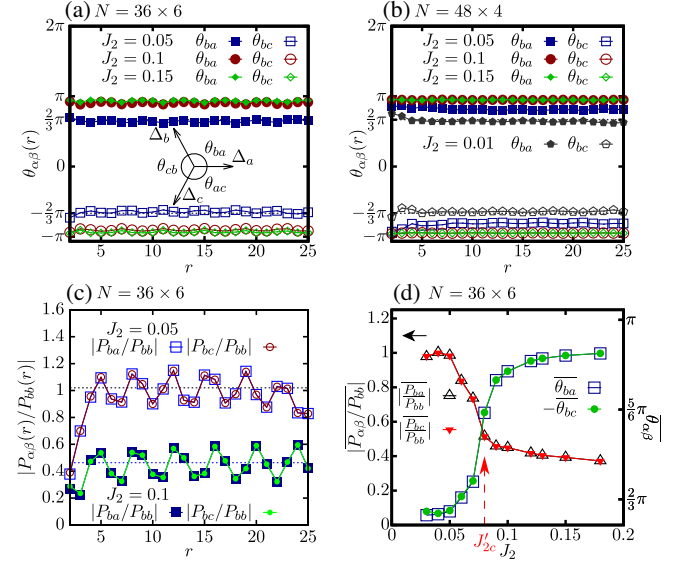


FIG. 5. Transition from the  $d + id$ -wave SC2 phases to SC0 phase. (a) The spatial dependence of relative phases for SC order parameters for various  $J_2$  on the  $L_y = 6$  ( $L_x = 36$ ) system.  $\mathbf{r}$  is chosen along the  $x$  direction  $\mathbf{r} = (r, 0)$ . (b) The relative phases for SC order parameters on the  $L_y = 4$  ( $L_x = 48$ ) system. (c) The ratio of the magnitudes of different SC correlations. The dashed line indicates the average over distances. (d) The spatial average values of the relative phases of SC order parameters and the ratios of magnitudes of different SC correlations for various  $J_2$ . All results are obtained at  $J_\chi = 0.05$  with bond dimension  $M = 10000$  ( $M = 8000$ ) on  $L_y = 6$  ( $L_y = 4$ ) systems. The doping level is  $\delta = 1/12$ .

for different nearest-neighbor bonds; see illustrations in the inset in Fig. 5(a). The pairing symmetry for different SC states is illustrated in Fig. 5(a) on  $N = 36 \times 6$  systems. At  $J_2 = J_\chi = 0.05$  in the SC2 regime,  $\theta_{\alpha\beta}(r)$  remains almost independent of  $r$ , and the phases for order parameters are nearly quantized to  $[\theta_{bb}, \theta_{bc}, \theta_{ba}] \approx [0, -0.64\pi, 0.65\pi] \approx [0, -\frac{2}{3}\pi, \frac{2}{3}\pi]$ , which represents an isotropic  $d + id$  wave with  $C_3$  rotational symmetry. The angles  $\theta_{ba}$  and  $\theta_{bc}$  are closer to  $\pm 2\pi/3$  on wider system  $L_y = 6$  compared with  $L_y = 4$  results (with  $L_x = 48$ ) as shown in Figs. 5(a) and 5(b). At larger  $J_2 = 0.15$  with  $J_\chi = 0.05$  in the SC0 phase, these phases become  $[\theta_{bb}, \theta_{bc}, \theta_{ba}] \approx [0, -0.93\pi, 0.93\pi] \approx [0, -\pi, \pi]$ , which are nearly independent of  $L_y = 4$  or 6, suggesting a  $d$ -wave SC state consistent with the Chern number  $C = 0$  for this phase.

On the other hand, the relative strength of the SC correlations for different bonds also evolves with the increase of  $J_2$ . As shown in Fig. 5(c),  $|P_{ba}(r)/P_{bb}(r)|$  and  $|P_{bc}(r)/P_{bb}(r)|$  have spatial oscillations and remain almost a constant average as  $r$  increases, which suggests a power-law-decaying behavior of  $|P_{ba}(r)|$  and  $|P_{bc}(r)|$  with the same exponents  $K_{SC}$ . At smaller  $J_2 = 0.05$ , the ratios  $|P_{ba}(r)/P_{bb}(r)|$  and  $|P_{bc}(r)/P_{bb}(r)|$  are close to 1.0, while they drop to around 0.46 observed at  $J_2 = 0.1$ , keeping the

same  $J_x = 0.05$ . We further show an example of the SC1 phase at  $J_2 = 0.01$  and  $J_x = 0.05$  on  $L_y = 4$  in Fig. 5(b) with nearly quantized phases  $[\theta_{bb}, \theta_{bc}, \theta_{ba}] \approx [0, -0.64\pi, 0.64\pi] \approx [0, -\frac{2}{3}\pi, \frac{2}{3}\pi]$ . From mean-field theory, the isotropic SC1 state with  $C = 1$  has nodal quasiparticle excitations [42], and we leave the full nature of this state to future study due to the increased difficulty of converging the SC correlations for this critical phase on  $L_y = 6$ .

## IV. SYMMETRY EVOLUTION AND PHASE TRANSITIONS

### A. Evolution of the pairing order parameters

Now we focus on the symmetry evolution of the pairing order parameters from SC2 phases to SC0 phase. As shown in Fig. 5(d), the  $-\overline{\theta_{bc}}$  and  $\overline{\theta_{ba}}$  averaged over the middle 24 columns of the system with  $L_x = 36$  increase monotonically from  $\frac{2}{3}\pi$  toward  $\pi$  as  $J_2$  increases. At the same time, we find direct evidence of the increased nematicity as  $J_2$  increases, which is identified by the ratio of the magnitudes of SC pairing correlations for different bonds. As shown in Fig. 5(d), the spatial averaged ratios  $|\overline{P_{ba}/P_{bb}}|$  and  $|\overline{P_{bc}/P_{bb}}|$  decrease monotonically from 1 to around 0.4 at the larger  $J_2$  side. A transition from an isotropic TSC phase to a nematic SC phase takes place inside the SC2 regime as indicated by the arrow in Fig. 5(d) pointing to a critical  $J_{2c}'$ , where both the  $|\overline{P_{ba}/P_{bb}}|$  and  $|\overline{P_{bc}/P_{bb}}|$  decrease quickly to the near-saturated value. This feature revealed by the nematicity evolution shows a transition inside the SC2 regime, indicating that a nematic TSC phase emerges for  $J_{2c}' < J_2 < J_{2c}^{(2)}$ . As shown in Fig. 1(b), we identify a finite regime with increased nematicity in the SC pairing correlations, while its topological nature remains the same with the Chern number  $C = 2$ , which is consistent with a nematic TSC state emerging within the  $C = 2$  class of SC phases. The phase boundary is determined by the quick increase of  $\overline{\theta_{ba}}$  to around  $\frac{5}{6}\pi$ . The emergent nematic TSC state is an analog state to the nematic fractional quantum Hall state with gapless collective excitations [65–68]. With further increase of  $J_2$ , the topological quantum phase transition takes place where the nematic  $d$ -wave SC state is recovered in the SC0 phase.

### B. Nature of quantum phase transitions

We now explore the nature of quantum phase transitions by following the energy and entanglement entropy evolution along the parameter line of  $J_x = 0.05$ . To calculate the entanglement entropy  $S$ , the cylinder is cut into two equal halves, and  $S$  is obtained from the eigenvalues  $\lambda_i$  of the reduced density matrix  $S = -\sum_i \lambda_i \log(\lambda_i)$ . As shown in Fig. 6(a), the energy per site  $E_0$  shows a small kink, and the entropy  $S$  shows a large jump at  $J_{2c}^{(1)} \approx 0.021$ , which is very

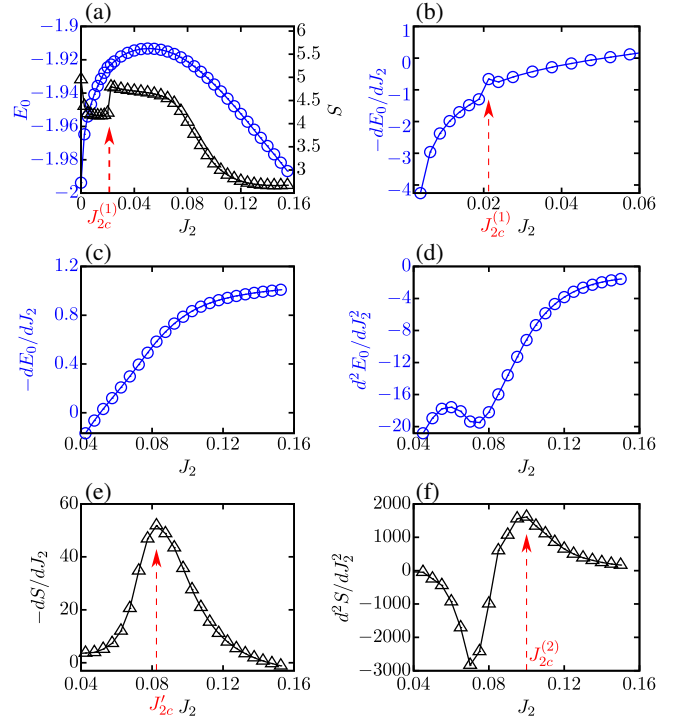


FIG. 6. The energy per site  $E_0$  and entanglement entropy  $S$  for various  $J_2$  obtained at fixed  $J_x = 0.05$  on a  $N = 16 \times 6$  cylinder. (a) The energy and entanglement entropy where  $J_{2c}^{(1)}$  is identified from the small jump in  $S$ . (b) The first-order derivative of  $E_0$  with respect to  $J_2$  where  $J_{2c}^{(1)}$  is identified at the discontinuity point. (c) The first-order derivative of  $E_0$  for larger  $J_2$ . (d) The second-order derivative of  $E_0$  for larger  $J_2$ . (e) The first-order derivative of  $S$  where  $J_{2c}'$  is identified as the peak. (f) The second-order derivative of  $S$  where  $J_{2c}^{(2)}$  is identified as the peak. The results are obtained with  $M = 10000$ . The doping level is  $\delta = 1/12$ .

close to the transition point between  $C = 1$  and  $C = 2$  phases, indicating a first-order transition between SC1 and the isotropic TSC (SC2) phase. The first-order transition is further revealed by  $-dE_0/dJ_2$  given in Fig. 6(b), which shows discontinuity around  $J_{2c}^{(1)}$ . Two other transitions from the isotropic TSC to nematic TSC and from nematic TSC to  $d$ -wave SC are continuous transitions with smooth evolution of  $E_0$  and  $S$  [Fig. 6(a)] and their derivatives [Figs. 6(c)–6(f)]. Interestingly, the transition point between the isotropic TSC and nematic TSC is indicated by the peak in  $-dS/dJ_2$ , which is very close to the one identified by the nematicity in SC pairing correlations. The transition between nematic TSC and nematic  $d$ -wave SC may be identified by the peak in  $d^2S/dJ_2^2$ , which is shifted from the one identified by the Chern number with flux insertion into a very long cylinder studied in the infinite DMRG. This may be explained by the finite size effect for identifying higher-order transitions where the peaks in entropy usually shift with system lengths [72,73].

### C. Evolution of the spin correlations

The evolution of spin correlations can be studied through the spin structure factor defined as  $S(\mathbf{k}) = (1/N') \sum_{i,j} \langle \mathbf{S}_i \cdot \mathbf{S}_j \rangle e^{i\mathbf{k} \cdot (\mathbf{r}_i - \mathbf{r}_j)}$  for a system with  $N = 36 \times 6$ , where  $i$  and  $j$  are summed over the middle  $N' = 2L_y \times L_y$  sites to avoid boundary effects. As shown in Fig. 7(a),  $S(\mathbf{k})$  has strong peaks at the  $\mathbf{K}$  points representing strong  $120^\circ$  AFM fluctuations at short distances for  $J_2 = 0.01, J_\chi = 0.05$  inside the SC1 phase, while the spin correlations exponentially decay at long distance for all three classes of SC phases (see Supplemental Sec. III E [62] for details). With a larger  $J_2 = 0.05$  in the SC2 phase,  $S(\mathbf{k})$  becomes nearly featureless with some intensity around the Brillouin zone boundaries as shown in Figs. 7(b) and 7(c), which is consistent with an isotropic  $d + id$ -wave TSC state. As  $J_2$  further increases to 0.1, moderate peaks appear in  $S(\mathbf{k})$  at the  $\mathbf{M}$  points with nematicity as seen in Figs. 7(d) and 7(e), where the SC pairing order parameters also become anisotropic [Fig. 5(d)]. Further increasing  $J_2$  into the SC0 phase, the spin fluctuations appear as brighter peaks in  $S(\mathbf{k})$  at the  $\mathbf{M}$  points, with stronger stripe fluctuations as shown in Fig. 7(f). The emerging picture is that the spin nematicity tuned by hole dynamics (see more details in Supplemental Sec. IV [62]) and spin interactions with the increase of  $J_2$  (and  $t_2$ ) are the determining forces in driving the quantum phase transitions between different SC phases.

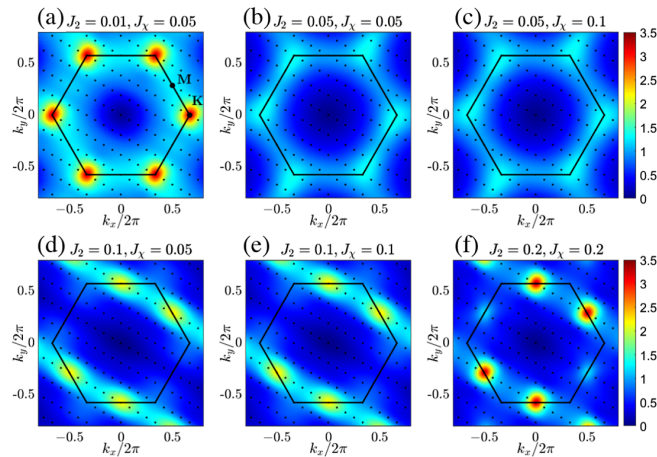


FIG. 7. The spin structure factor  $S(\mathbf{k})$  obtained on an  $N = 36 \times 6$  cylinder using correlations from middle  $N' = 12 \times 6$  sites. (a) SC1 phase at  $J_2 = 0.01$ . (b),(c) Isotropic  $d + id$ -wave TSC phase at  $J_2 = 0.05$  with near-isotropic structure. (d),(e) Nematic TSC phase at  $J_2 = 0.1$ . (f) SC0 state at  $J_2 = 0.2$ . The first Brillouin zone is indicated by the solid line with the  $\mathbf{M}$  and  $\mathbf{K}$  points marked, and the black dots represent the allowed discrete momenta for the finite system with  $12 \times 6$  sites. The results are obtained with  $M = 10000$ . The doping level is  $\delta = 1/12$ .

### V. SUMMARY AND DISCUSSION

We have extensively studied the ground state of the lightly doped extended  $t$ - $J$ - $J_\chi$  model on triangular lattice based on the state-of-the-art DMRG method and uncovered a global picture of emergent unconventional superconductivity in systems with chiral interactions that could be induced by an external magnetic field [32]. We identify three classes of superconducting phases (SC1, SC2, and SC0) characterized by different topological Chern numbers and pairing symmetries. As next-nearest-neighbor hopping  $t_2$  and the related spin coupling  $J_2$  increase, the critical SC1 state with Chern number  $C = 1$  has a transition to the isotropic TSC phase, which is a gapped topological  $d + id$ -wave superconductor with  $C = 2$ . With further increase of  $t_2$  and  $J_2$ , the isotropic TSC state has a transition to a nematic TSC state in the smaller  $J_\chi$  regime, which is an analogy of the nematic fractional quantum Hall state with broken rotational symmetry [66–68]. A topological phase transition from the  $C = 2$  TSC states to the nematic  $d$ -wave SC0 state with  $C = 0$  occurs for larger  $t_2$  and  $J_2$ . The hole dynamics tuned by next-nearest-neighboring hoppings and spin couplings drives the topological quantum phase transitions between different SC phases, and a small chiral interaction  $J_\chi \approx 0.01$  stabilizes the SC states.

The TSC is a long-sought state, and it was conjectured that such a SC state may be realized by doping a CSL [48,49] if it can win over other competing states varying from a chiral metal [11,34] to a fractionalized Wigner crystal [57,74]. Despite intensive efforts in searching for such a TSC state in strongly correlated systems during the past decades, there is only one established example by unbiased numerical studies of the  $t$ - $J$ - $J_\chi$  model [32]. The identified TSC state also showed some instability on a wider cylinder ( $L_y = 6$ ) [32] before adding next-nearest-neighboring hopping, indicating that it is near a phase boundary. In this work, we uncover a global phase diagram for the same model and unravel two distinct classes of TSC phases with Chern numbers  $C = 1, 2$  and a nematic  $d$ -wave SC phase with  $C = 0$ . The new insight to the mechanism of the doping-induced TSC is that the TSC can emerge by doping a correlated Mott insulating state with  $120^\circ$  AFM besides doping a CSL state. Importantly, the hole dynamics changes the spin background and induces a topological quantum phase transition upon doping a magnetic ordered state, widening the opportunity for discovering TSC in triangular compounds. On the other hand, nematic SC with  $C = 0$  can emerge from either doping the CSL or magnetic ordered states [53], suggesting the rich interplay between unconventional SC and spin background.

A recent analytical study [46] has identified topological and nematic SC in the moiré superlattice of twisted bilayer TMD that realizes an effective triangular lattice model with repulsive interactions. While the study addresses the physics in the weak coupling picture with spin-valley fluctuations, it is interesting to see the  $C = 2$  topological



$d + id$ -wave SC and the nematic  $d$ -wave SC being discovered, which may indicate a possible universal picture for SC on triangular lattice with repulsive interactions. It would be exciting to examine the extended Hubbard model with short-range Coulomb interactions for such systems from weak to strong couplings [7], which can make further predictions for TMD systems. In light of the theoretical prediction of the SU(4) CSL [75] in time-reversal-invariant TMD bilayers, we anticipate TSC to be a strong competing state and a rich phase diagram to be revealed. Besides the triangular lattice, it will also be interesting to search for possible TSC states in other systems including kagome compounds, where Mott insulators show similar rich physics with emergent CSL [52].

### ACKNOWLEDGMENTS

We thank Z. Q. Wang and Yahui Zhang for stimulating discussions. This work was supported by the U.S. Department of Energy, Office of Basic Energy Sciences under Grant No. DE-FG02-06ER46305.

- 
- [1] P. W. Anderson, *The Resonating Valence Bond State in La<sub>2</sub>CuO<sub>4</sub> and Superconductivity*, *Science* **235**, 1196 (1987).
- [2] P. A. Lee, N. Nagaosa, and X.-G. Wen, *Doping a Mott Insulator: Physics of High-Temperature Superconductivity*, *Rev. Mod. Phys.* **78**, 17 (2006).
- [3] B. Keimer, S. A. Kivelson, M. R. Norman, S. Uchida, and J. Zaanen, *From Quantum Matter to High-Temperature Superconductivity in Copper Oxides*, *Nature (London)* **518**, 179 (2015).
- [4] C. Proust and L. Taillefer, *The Remarkable Underlying Ground States of Cuprate Superconductors*, *Annu. Rev. Condens. Matter Phys.* **10**, 409 (2019).
- [5] M. Ogata and H. Fukuyama, *The  $t$ - $j$  Model for the Oxide High-Tc Superconductors*, *Rep. Prog. Phys.* **71**, 036501 (2008).
- [6] E. Fradkin, S. A. Kivelson, and J. M. Tranquada, *Colloquium: Theory of Intertwined Orders in High Temperature Superconductors*, *Rev. Mod. Phys.* **87**, 457 (2015).
- [7] D. P. Arovas, E. Berg, S. A. Kivelson, and S. Raghu, *The Hubbard Model*, *Annu. Rev. Condens. Matter Phys.* **13**, 239 (2022).
- [8] L. Balents, *Spin Liquids in Frustrated Magnets*, *Nature (London)* **464**, 199 (2010).
- [9] T. Senthil and P. A. Lee, *Cuprates as Doped U(1) Spin Liquids*, *Phys. Rev. B* **71**, 174515 (2005).
- [10] Z. Y. Weng, D. N. Sheng, and C. S. Ting, *Mean-Field Description of the Phase String Effect in the  $t$ - $j$  Model*, *Phys. Rev. B* **59**, 8943 (1999).
- [11] X.-Y. Song, A. Vishwanath, and Y.-H. Zhang, *Doping the Chiral Spin Liquid: Topological Superconductor or Chiral Metal*, *Phys. Rev. B* **103**, 165138 (2021).
- [12] S. R. White and D. J. Scalapino, *Pairing on Striped  $t$ - $t'$ - $j$  Lattices*, *Phys. Rev. B* **79**, 220504(R) (2009).
- [13] P. Corboz, T. M. Rice, and M. Troyer, *Competing States in the  $t$ - $j$  Model: Uniform  $d$ -Wave State versus Stripe State*, *Phys. Rev. Lett.* **113**, 046402 (2014).
- [14] J. P. F. LeBlanc *et al.* (Simons Collaboration on the Many-Electron Problem), *Solutions of the Two-Dimensional Hubbard Model: Benchmarks and Results from a Wide Range of Numerical Algorithms*, *Phys. Rev. X* **5**, 041041 (2015).
- [15] H.-C. Jiang and T. P. Devereaux, *Superconductivity in the Doped Hubbard Model and Its Interplay with Next-Nearest Hopping  $t'$* , *Science* **365**, 1424 (2019).
- [16] M. Qin, C.-M. Chung, H. Shi, E. Vitali, C. Hubig, U. Schollwöck, S. R. White, and S. Zhang (Simons Collaboration on the Many-Electron Problem), *Absence of Superconductivity in the Pure Two-Dimensional Hubbard Model*, *Phys. Rev. X* **10**, 031016 (2020).
- [17] B.-X. Zheng, C.-M. Chung, P. Corboz, G. Ehlers, M.-P. Qin, R. M. Noack, H. Shi, S. R. White, S. Zhang, and G. K.-L. Chan, *Stripe Order in the Underdoped Region of the Two-Dimensional Hubbard Model*, *Science* **358**, 1155 (2017).
- [18] H.-C. Jiang, Z.-Y. Weng, and S. A. Kivelson, *Superconductivity in the Doped  $t$ - $j$  Model: Results for Four-Leg Cylinders*, *Phys. Rev. B* **98**, 140505(R) (2018).
- [19] J. F. Dodaro, H.-C. Jiang, and S. A. Kivelson, *Intertwined Order in a Frustrated Four-Leg  $t$ - $j$  Cylinder*, *Phys. Rev. B* **95**, 155116 (2017).
- [20] Y.-F. Jiang, J. Zaanen, T. P. Devereaux, and H.-C. Jiang, *Ground State Phase Diagram of the Doped Hubbard Model on the Four-Leg Cylinder*, *Phys. Rev. Research* **2**, 033073 (2020).
- [21] H.-C. Jiang and S. A. Kivelson, *High Temperature Superconductivity in a Lightly Doped Quantum Spin Liquid*, *Phys. Rev. Lett.* **127**, 097002 (2021).
- [22] S. Gong, W. Zhu, and D. N. Sheng, *Robust  $d$ -Wave Superconductivity in the Square-Lattice  $t - j$  Model*, *Phys. Rev. Lett.* **127**, 097003 (2021).
- [23] S. Jiang, D. J. Scalapino, and S. R. White, *Ground-State Phase Diagram of the  $tt'$ - $j$  Model*, *Proc. Natl. Acad. Sci. U.S.A.* **118**, e2109978118 (2021).
- [24] S. R. White, *Density Matrix Formulation for Quantum Renormalization Groups*, *Phys. Rev. Lett.* **69**, 2863 (1992).
- [25] G. Baskaran, *Electronic Model for CoO<sub>2</sub> Layer Based Systems: Chiral Resonating Valence Bond Metal and Superconductivity*, *Phys. Rev. Lett.* **91**, 097003 (2003).
- [26] B. Kumar and B. S. Shastry, *Superconductivity in CoO<sub>2</sub> Layers and the Resonating Valence Bond Mean-Field Theory of the Triangular Lattice  $t$ - $j$  Model*, *Phys. Rev. B* **68**, 104508 (2003).
- [27] Q.-H. Wang, D.-H. Lee, and P. A. Lee, *Doped  $t$ - $j$  Model on a Triangular Lattice: Possible Application to Na <sub>$x$</sub> CoO<sub>2</sub> ·  $y$ H<sub>2</sub>O and Na<sub>1- $x$</sub> TiO<sub>2</sub>*, *Phys. Rev. B* **69**, 092504 (2004).
- [28] O. I. Motrunich and P. A. Lee, *Possible Effects of Charge Frustration in Na <sub>$x$</sub> CoO<sub>2</sub>: Bandwidth Suppression, Charge Orders, and Resurrected Resonating Valence Bond Superconductivity*, *Phys. Rev. B* **69**, 214516 (2004).
- [29] S. Raghu, S. A. Kivelson, and D. J. Scalapino, *Superconductivity in the Repulsive Hubbard Model: An Asymptotically Exact Weak-Coupling Solution*, *Phys. Rev. B* **81**, 224505 (2010).

- [30] K. S. Chen, Z. Y. Meng, U. Yu, S. Yang, M. Jarrell, and J. Moreno, *Unconventional Superconductivity on the Triangular Lattice Hubbard Model*, *Phys. Rev. B* **88**, 041103(R) (2013).
- [31] J. Venderley and E.-A. Kim, *Density Matrix Renormalization Group Study of Superconductivity in the Triangular Lattice Hubbard Model*, *Phys. Rev. B* **100**, 060506(R) (2019).
- [32] Y.-F. Jiang and H.-C. Jiang, *Topological Superconductivity in the Doped Chiral Spin Liquid on the Triangular Lattice*, *Phys. Rev. Lett.* **125**, 157002 (2020).
- [33] H.-C. Jiang, *Superconductivity in the Doped Quantum Spin Liquid on the Triangular Lattice*, *npj Quantum Mater.* **6**, 71 (2021).
- [34] Z. Zhu, D. N. Sheng, and A. Vishwanath, *Doped Mott Insulators in the Triangular-Lattice Hubbard Model*, *Phys. Rev. B* **105**, 205110 (2022).
- [35] Y. Gannot, Y.-F. Jiang, and S. A. Kivelson, *Hubbard Ladders at Small  $u$  Revisited*, *Phys. Rev. B* **102**, 115136 (2020).
- [36] A. Szasz, J. Motruk, M. P. Zaletel, and J. E. Moore, *Chiral Spin Liquid Phase of the Triangular Lattice Hubbard Model: A Density Matrix Renormalization Group Study*, *Phys. Rev. X* **10**, 021042 (2020).
- [37] B.-B. Chen, Z. Chen, S.-S. Gong, D. Sheng, W. Li, and A. Weichselbaum, *Quantum Spin Liquid with Emergent Chiral Order in the Triangular-Lattice Hubbard Model*, arXiv:2102.05560.
- [38] C. Peng, Y.-F. Jiang, Y. Wang, and H.-C. Jiang, *Gapless Spin Liquid and Pair Density Wave of the Hubbard Model on Three-Leg Triangular Cylinders*, *New J. Phys.* **23**, 123004 (2021).
- [39] A. Wietek, R. Rossi, F. Šimkovic, M. Klett, P. Hansmann, M. Ferrero, E. M. Stoudenmire, T. Schäfer, and A. Georges, *Mott Insulating States with Competing Orders in the Triangular Lattice Hubbard Model*, *Phys. Rev. X* **11**, 041013 (2021).
- [40] A. M. Aghaei, B. Bauer, K. Shtengel, and R. V. Mishmash, *Efficient Matrix-Product-State Preparation of Highly Entangled Trial States: Weak Mott Insulators on the Triangular Lattice Revisited*, arXiv:2009.12435.
- [41] K. Takada, H. Sakurai, E. Takayama-Muromachi, F. Izumi, R. A. Dilanian, and T. Sasaki, *Superconductivity in Two-Dimensional  $\text{CoO}_2$  Layers*, *Nature (London)* **422**, 53 (2003).
- [42] S. Zhou and Z. Wang, *Nodal  $d+id$  Pairing and Topological Phases on the Triangular Lattice of  $\text{Na}_x\text{CoO}_2\cdot y\text{H}_2\text{O}$ : Evidence for an Unconventional Superconducting State*, *Phys. Rev. Lett.* **100**, 217002 (2008).
- [43] F. Wu, T. Lovorn, E. Tutuc, and A. H. MacDonald, *Hubbard Model Physics in Transition Metal Dichalcogenide Moiré Bands*, *Phys. Rev. Lett.* **121**, 026402 (2018).
- [44] Y. Tang, L. Li, T. Li, Y. Xu, S. Liu, K. Barmak, K. Watanabe, T. Taniguchi, A. H. MacDonald, J. Shan, and K. F. Mak, *Simulation of Hubbard Model Physics in  $\text{WSe}_2/\text{WS}_2$  Moiré Superlattices*, *Nature (London)* **579**, 353 (2020).
- [45] L. An, X. Cai, D. Pei, M. Huang, Z. Wu, Z. Zhou, J. Lin, Z. Ying, Z. Ye, X. Feng *et al.*, *Interaction Effects and Superconductivity Signatures in Twisted Double-Bilayer  $\text{WSe}_2$* , *Nanoscale Horiz.* **5**, 1309 (2020).
- [46] C. Schrade and L. Fu, *Nematic, Chiral and Topological Superconductivity in Transition Metal Dichalcogenides*, arXiv:2110.10172.
- [47] M. M. Scherer, D. M. Kennes, and L. Classen,  *$N = 4$  Chiral Superconductivity in Moiré Transition Metal Dichalcogenides*, arXiv:2108.11406.
- [48] V. Kalmeyer and R. B. Laughlin, *Equivalence of the Resonating-Valence-Bond and Fractional Quantum Hall States*, *Phys. Rev. Lett.* **59**, 2095 (1987).
- [49] X.-G. Wen, F. Wilczek, and A. Zee, *Chiral Spin States and Superconductivity*, *Phys. Rev. B* **39**, 11413 (1989).
- [50] B. Bauer, L. Cincio, B. Keller, M. Dolfi, G. Vidal, S. Trebst, and A. Ludwig, *Chiral Spin Liquid and Emergent Anyons in a Kagome Lattice Mott Insulator*, *Nat. Commun.* **5**, 5137 (2014).
- [51] Y.-C. He, D. N. Sheng, and Y. Chen, *Chiral Spin Liquid in a Frustrated Anisotropic Kagome Heisenberg Model*, *Phys. Rev. Lett.* **112**, 137202 (2014).
- [52] S.-S. Gong, W. Zhu, and D. N. Sheng, *Emergent Chiral Spin Liquid: Fractional Quantum Hall Effect in a Kagome Heisenberg model*, *Sci. Rep.* **4**, 6317 (2014).
- [53] S.-S. Gong, W. Zhu, J.-X. Zhu, D. N. Sheng, and K. Yang, *Global Phase Diagram and Quantum Spin Liquids in a Spin-1/2 Triangular Antiferromagnet*, *Phys. Rev. B* **96**, 075116 (2017).
- [54] A. Wietek and A. M. Läuchli, *Chiral Spin Liquid and Quantum Criticality in Extended  $s = 1/2$  Heisenberg Models on the Triangular Lattice*, *Phys. Rev. B* **95**, 035141 (2017).
- [55] R. B. Laughlin, *Superconducting Ground State of Non-interacting Particles Obeying Fractional Statistics*, *Phys. Rev. Lett.* **60**, 2677 (1988).
- [56] D.-H. Lee and M. P. A. Fisher, *Anyon Superconductivity and the Fractional Quantum Hall Effect*, *Phys. Rev. Lett.* **63**, 903 (1989).
- [57] H.-C. Jiang, T. Devereaux, and S. A. Kivelson, *Holon Wigner Crystal in a Lightly Doped Kagome Quantum Spin Liquid*, *Phys. Rev. Lett.* **119**, 067002 (2017).
- [58] N. Read and D. Green, *Paired States of Fermions in Two Dimensions with Breaking of Parity and Time-Reversal Symmetries and the Fractional Quantum Hall Effect*, *Phys. Rev. B* **61**, 10267 (2000).
- [59] T. Senthil, J. B. Marston, and M. P. A. Fisher, *Spin Quantum Hall Effect in Unconventional Superconductors*, *Phys. Rev. B* **60**, 4245 (1999).
- [60] A. Luther and V. Emery, *Backward Scattering in the One-Dimensional Electron Gas*, *Phys. Rev. Lett.* **33**, 589 (1974).
- [61] I. P. McCulloch, *From Density-Matrix Renormalization Group to Matrix Product States*, *J. Stat. Mech.* (2007) P10014.
- [62] See Supplemental Material at <http://link.aps.org/supplemental/10.1103/PhysRevX.12.031009> for detailed numerical results.
- [63] A. G. Grushin, J. Motruk, M. P. Zaletel, and F. Pollmann, *Characterization and Stability of a Fermionic  $\nu = 1/3$  Fractional Chern Insulator*, *Phys. Rev. B* **91**, 035136 (2015).
- [64] For  $J_2 < 0.01$  or  $J_\chi < 0.01$ , it becomes increasingly difficult to obtain a converged ground state or identify phase boundaries.

- [65] F. D. M. Haldane, *Geometrical Description of the Fractional Quantum Hall Effect*, *Phys. Rev. Lett.* **107**, 116801 (2011).
- [66] Y. You, G. Y. Cho, and E. Fradkin, *Theory of Nematic Fractional Quantum Hall States*, *Phys. Rev. X* **4**, 041050 (2014).
- [67] B. Yang, C. H. Lee, C. Zhang, and Z.-X. Hu, *Anisotropic Pseudopotential Characterization of Quantum Hall Systems under a Tilted Magnetic Field*, *Phys. Rev. B* **96**, 195140 (2017).
- [68] N. Regnault, J. Maciejko, S. A. Kivelson, and S. L. Sondhi, *Evidence of a Fractional Quantum Hall Nematic Phase in a Microscopic Model*, *Phys. Rev. B* **96**, 035150 (2017).
- [69] D. N. Sheng, Z. Y. Weng, L. Sheng, and F. D. M. Haldane, *Quantum Spin-Hall Effect and Topologically Invariant Chern Numbers*, *Phys. Rev. Lett.* **97**, 036808 (2006).
- [70] W.-J. Hu, W. Zhu, Y. Zhang, S. Gong, F. Becca, and D. N. Sheng, *Variational Monte Carlo Study of a Chiral Spin Liquid in the Extended Heisenberg Model on the Kagome Lattice*, *Phys. Rev. B* **91**, 041124(R) (2015).
- [71] U. Schollwöck, *The Density-Matrix Renormalization Group in the Age of Matrix Product States*, *Ann. Phys. (Amsterdam)* **326**, 96 (2011).
- [72] G.-Q. Zhong, S.-S. Gong, Q.-R. Zheng, and G. Su, *Quantum Phase Transitions in a Spin-1/2 Alternating Heisenberg Antiferromagnetic Chain under a Staggered Transverse Magnetic Field*, *Phys. Lett. A* **373**, 1687 (2009).
- [73] J. Zhang, *Fidelity and Entanglement Entropy for Infinite-Order Phase Transitions*, *Phys. Rev. B* **104**, 205112 (2021).
- [74] C. Peng, Y. Jiang, D. Sheng, and H. Jiang, *Doping Quantum Spin Liquids on the Kagome Lattice*, *Adv. Quantum Technol.* **4**, 2000126 (2021).
- [75] Y.-H. Zhang, D. N. Sheng, and A. Vishwanath, *SU(4) Chiral Spin Liquid, Exciton Supersolid, and Electric Detection in Moiré Bilayers*, *Phys. Rev. Lett.* **127**, 247701 (2021).